ADVANCED MATERIALS
www.advmat.de

Highly Tunable Relaxors Developed from Antiferroelectrics

Hao Pan, Liyan Wu, John Carroll, Menglin Zhu, Zishen Tian, Dongfang Chen, Hongrui Zhang, Xianzhe Chen, Xiaoxi Huang, Irina Baraban, Sreekeerthi Pamula, Cedric J. G. Meyers, R. Ramesh, Kathleen Coleman, Brendan Hanrahan, James M. LeBeau, Jonathan E. Spanier, and Lane W. Martin**

Highly responsive, voltage-tunable dielectrics are essential for microwave-telecommunication electronics. Ferroelectric/relaxor materials have been leading candidates for such functionality and have exhibited agile dielectric responses. Here, it is demonstrated that relaxor materials developed from antiferroelectrics can achieve both ultrahigh dielectric response and tunability. The system, based on alloying the archetypal antiferroelectric $PbZrO_3$ with the dielectric $BaZrO_3$, exhibits a more complex phase evolution than that in traditional relaxors and is characterized by an unconventional multi-phase competition between antiferroelectric, ferroelectric, and paraelectric order. This interplay of phases can greatly enhance the local heterogeneities and results in relaxor characteristics while preserving considerable polarizability. Upon studying $Pb_{1-x}Ba_xZrO_3$ for $x = 0$-0.45, $Pb_{0.65}Ba_{0.35}ZrO_3$ is found to provide for exceptional dielectric tunability under low bias fields (≈81% at 200 kV cm^{-1} and ≈91% at 500 kV cm^{-1}) at 10 kHz, outcompeting most traditional relaxor ferroelectric films. This high tunability is sustained in the radio-frequency range, resulting in a high commutation quality factor (>2000 at 1 GHz). This work highlights the phase evolution from antiferroelectrics (with lower, "positive" dielectric tunability) to relaxors (with higher, "negative" tunability), underscoring a promising approach to develop relaxors with enhanced functional capabilities and new possibilities.

1. Introduction

The continuous development of electronics, including their further miniaturization and integration in circuits/devices, requires functional materials with large electrical responses and low-energy dissipation.[1–4] For example, advances in wireless communications (e.g., cell phones, 5G networks, internet-of-things, etc.) relies heavily on radio-frequency phase shifters, wave filters, and other devices in which the capacitance and resonant frequency can be finely regulated (tuned) by an applied voltage.[5–7] For such applications, tunable dielectrics (especially in thin-film form to reduce the operating voltage) have garnered considerable interest, among which ferroelectric materials have been extensively pursued because of their nonlinear dielectric response with high tunability [$(\varepsilon_{r,0} - \varepsilon_{r,E})/\varepsilon_{r,0}$, where $\varepsilon_{r,0}$ and $\varepsilon_{r,E}$ are the relative permittivity (dielectric constant) values at zero and a bias electric field E, respectively, with $\varepsilon_{r,0}$ normally being larger

H. Pan[+], Z. Tian, H. Zhang, X. Chen, X. Huang, S. Pamula, R. Ramesh
Department of Materials Science and Engineering
University of California
Berkeley, California 94720, USA
E-mail: panh@pku.edu.cn

L. Wu, D. Chen, C. J. G. Meyers, J. E. Spanier
Departments of Mechanical Engineering and Mechanics
Drexel University
Philadelphia, PA 19104, USA

J. Carroll, J. E. Spanier
Department of Electrical and Computer Engineering
Drexel University
Philadelphia, PA 19104, USA

J. Carroll
DEVCOM C5ISR U.S. Army
Aberdeen Proving Grounds, MD 21005, USA

The ORCID identification number(s) for the author(s) of this article can be found under https://doi.org/10.1002/adma.202505376

[+]Present address: School of Advanced Materials, Shenzhen Graduate School, Peking University, Shenzhen 518055, China

DOI: 10.1002/adma.202505376

M. Zhu, J. M. LeBeau
Department of Materials Science and Engineering
Massachusetts Institute of Technology
Cambridge, Massachusetts 02139, USA

Z. Tian, S. Pamula, R. Ramesh, L. W. Martin
Rice Advanced Materials Institute
Rice University
Houston, Texas 77005, USA
E-mail: lwmartin@rice.edu

X. Chen, R. Ramesh, L. W. Martin
Materials Sciences Division
Lawrence Berkeley National Laboratory
Berkeley, California 94720, USA

I. Baraban, J. E. Spanier
Departments of Physics
Drexel University
Philadelphia, PA 19104, USA

R. Ramesh, L. W. Martin
Departments of Materials Science and NanoEngineering and Physics and Astronomy
Rice University
Houston, Texas 77005, USA

than $\varepsilon_{r,E}$].[8,9] As compared to typical ferroelectrics (e.g., $BaTiO_3$), solid solutions such as $Ba_{1-x}Sr_xTiO_3$ in which the ferroelectric Curie temperature is chemically tuned below the operating temperature range, exhibit lower hysteresis and more agile dielectric/polarization responses providing further advantage of high tunability and low-energy dissipation.[6] Many other potential tunable dielectrics have also been explored in systems such as $BaTi_{1-x}Zr_xO_3$,[10] $PbMg_{1/3}Nb_{2/3}O_3$,[11] $(SrTiO_3)_{n-m}(BaTiO_3)_mSrO$,[7] etc., which show relaxor-like nature (i.e., slim polarization loops, low remanent polarization, and low hysteresis) originating from the presence of multiple cations on the equivalent sites which acts to destabilize the parent ferroelectric and, in turn, cause a competition between paraelectric and ferroelectric phases, as well as a breakdown of the long-range polar order (which has even been reported to produce polar nanodomains).[12,13] This approach of starting from a prototypical ferroelectric (e.g., $BaTiO_3$, $PbTiO_3$, $BiFeO_3$, etc.) and subsequently incorporating heterogenous cations (in the form of a solid solution) to disrupt the ferroelectric polar order with a paraelectric phase has been one of the primary pathways to develop highly responsive materials and even new relaxors for various functionalities.[14,15] The introduction of too much of the paraelectric phase, however, can degrade the polarizability, causing a compromise between the dielectric/polarization responsiveness and the hysteresis loss and energy dissipation.

On the other hand, antiferroelectrics (e.g., $PbZrO_3$), with antipolar order (at zero field) that can be switched to polar, ferroelectric order with applied field,[16,17] have also been demonstrated to be candidates for tunable dielectrics; albeit with "positive" tunability (i.e., $\varepsilon_{r,E} > \varepsilon_{r,0}$), because of the field-induced reversible antiferroelectric-to-ferroelectric transition and the corresponding double-hysteresis polarization loops.[18] To promote antiferroelectrics toward practical applications, it is also imperative to improve their responsiveness and reduce the energy dissipation (as in relaxor materials), through engineering of properties such as the antiferroelectric-to-ferroelectric transition (threshold) field and by reducing the polarization hysteresis at high fields.[19,20] Efforts have shown the possibility of such control by tuning the antiferroelectric-to-ferroelectric phase competition using defects, orientation, thickness, interfaces, etc.[21–24] Developing relaxor features has been demonstrated as another effective and a more universal approach to modulate antiferroelectrics, and can be realized by incorporating heterogenous cations to disrupt the antiferroelectric order (in a similar spirit to developing relaxors from prototypical ferroelectrics).[25–27] This method has been used to enhance antiferroelectric dielectric energy-storage capacity,[25,28,29] yet there has been a lack of focus on other functionalities such as the dielectric tunability. It is thus desirable to build a comprehensive understanding of this degree of freedom to design high-performance, low-loss phases from antiferroelectrics and to explore the new opportunities they can offer for advanced, responsive electronics, particularly in the realm of tunable dielectrics.

Here, starting from the prototypical antiferroelectric $PbZrO_3$, a relaxor phase was achieved by alloying it with $BaZrO_3$ such that the system undergoes a complex phase evolution with a combined antiferroelectric-to-ferroelectric transition and the emergence of relaxor features. Compared with conventional relaxors developed from ferroelectrics that exhibit merely a two-phase competition between ferroelectric and paraelectric order, $Pb_{1-x}Ba_xZrO_3$ (x = 0–0.45) films have a multi-phase competition among antiferroelectric, ferroelectric, and paraelectric order, which introduces greatly enhanced local heterogeneities and thus results in relaxor characteristics while preserving a significant proportion of the polar nature. In turn, $Pb_{0.65}Ba_{0.35}ZrO_3$ films are found to give optimal response and are able to reach ultrahigh dielectric tunability under relatively low bias fields (≈81% at 200 kV cm^{-1} and ≈91% at 500 kV cm^{-1}; both at 10 kHz), exceeding the performance of most conventional relaxor-ferroelectric films. This high tunability persists into the radio-frequency (GHz) range thus producing a high overall commutation quality factor (>2000 at 1 GHz). These observations shed light on the transition from typical antiferroelectrics to relaxor materials, highlighting the exceptional performance that provides new possibilities for applications with improved or extended functional capabilities.

2. Results and Discussion

A series of $Pb_{1-x}Ba_xZrO_3$ epitaxial films (x = 0-0.45; ≈100 nm in thickness) were synthesized on $DyScO_3$ $(110)_O$ substrates via pulsed-laser deposition (where O denotes orthorhombic indices). The films were fabricated through programmed alternating laser ablation of two ceramic targets (i.e., $PbZrO_3$ and $BaZrO_3$), which allows the materials to be homogeneously mixed at the sub-unit cell level and provides access to a range of compositions (Experimental Section). The $Pb_{1-x}Ba_xZrO_3$ compositions were controlled by changing the laser pulse numbers on each target (Table S1, Supporting Information). $SrRuO_3$ layers (30–45 nm thick) were also deposited as the bottom and top electrodes and fabricated into symmetric capacitor structures for (di)electric measurements (Experimental Section). The crystalline structure of the heterostructures was characterized using X-ray diffraction (**Figure 1** and Experimental Section). Due to the large lattice mismatch between $Pb_{1-x}Ba_xZrO_3$ (>4.10 Å) and the $DyScO_3$ substrates (≈ 3.95 Å), the films are relaxed (Figure S1, Supporting Information) and, by extension, there is insignificant epitaxial strain in the $Pb_{1-x}Ba_xZrO_3$ films. The $Pb_{1-x}Ba_xZrO_3$ films with $x \leq 0.15$ were found to maintain an orthorhombic phase structure with a majority $(240)_O$-orientation [i.e., $(200)_{pc}$] and a minority $(004)_O$- [i.e., $(002)_{pc}$] orientation (where "pc" denotes pseudocubic indices, with lattice parameters $b_o \approx 2a_o \approx 2\sqrt{2}a_{pc}$ and $c_o \approx 2c_{pc}$) in the X-ray line scans (bottom three datasets, Figure 1a) and consistent with the parent antiferroelectric $PbZrO_3$.[30] As

K. Coleman, B. Hanrahan
DEVCOM U.S. Army Research Laboratory
Adelphi, MD 20783, USA
J. E. Spanier
Department of Materials Science and Engineering
Drexel University
Philadelphia, PA 19104, USA
L. W. Martin
Department of Chemistry
Rice University
Houston, Texas 77005, USA

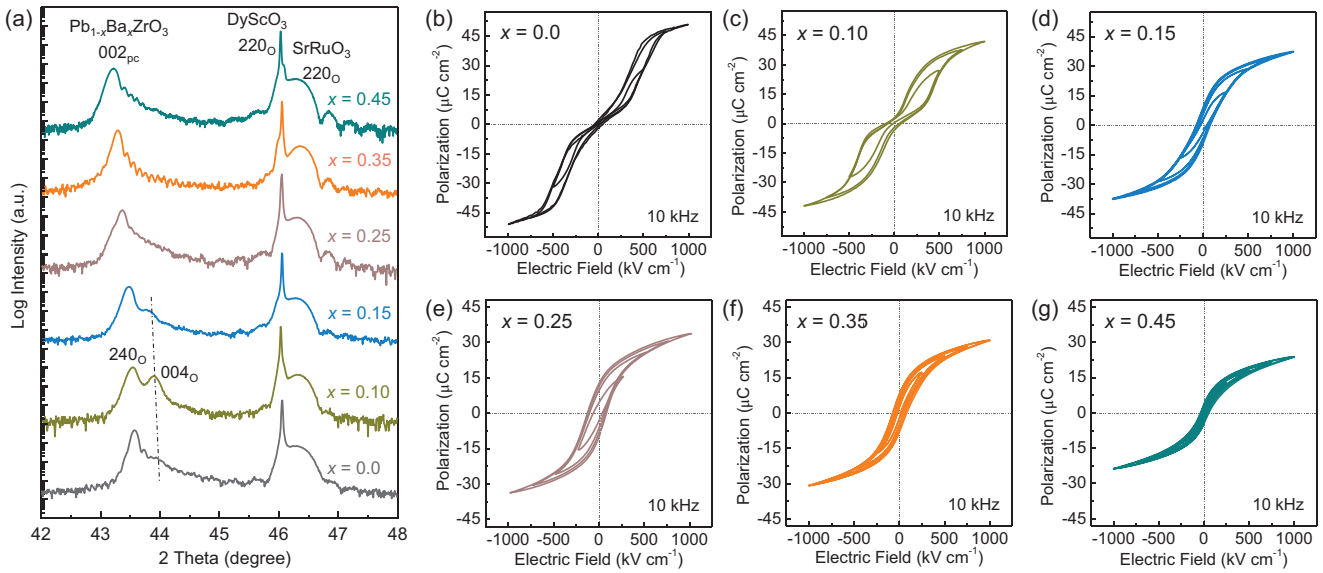

Figure 1. a) X-ray diffraction 2θ-ω scans for the $SrRuO_3/Pb_{1-x}Ba_xZrO_3/SrRuO_3/DyScO_3$ $(110)_O$ heterostructures with x increasing from 0 to 0.45. Polarization-electric-field hysteresis loops of the $Pb_{1-x}Ba_xZrO_3$ heterostructures with (b) $x = 0.0$ (pure $PbZrO_3$), c) $x = 0.10$, d) $x = 0.15$, e) $x = 0.25$, f) $x = 0.35$, and g) $x = 0.45$ measured at a frequency of 10 kHz.

x increases further, the two diffraction peaks gradually shift to lower angles and merge into one for $x \geq 0.25$ (top three datasets, Figure 1a). This agrees with the trend found in further reciprocal space mapping studies (Figure S1, Supporting Information), which demonstrate expansions in both a_{pc} and c_{pc} due to the introduction of the larger Ba^{2+} cations into the lead sites, and a gradual structural transition from orthorhombic to pseudocubic (with the a_{pc}/c_{pc} ratio systematically decreasing to 1.003 for $x = 0.45$, Table S2, Supporting Information). Such a structural transition is accompanied by a substantial change of polarization-switching behavior in the $Pb_{1-x}Ba_xZrO_3$ films. The films with $x = 0$ (Figure 1b) and 0.10 (Figure 1c) maintain typical antiferroelectric polarization switching with double-hysteresis loops, corresponding to four antiferroelectric-to-ferroelectric transition peaks in the switching curves (differential of polarization with respect to field, Figure S2 (Supporting Information). As x reaches and surpasses 0.15, the switching behaviors are found to evolve into single loops (Figure 1e–g) with only two polarization switching peaks (Figure S2, Supporting Information), indicating a phase transition to a ferroelectric state. It is noted that the $x = 0.15$ films exhibit coexisting behavior with predominant ferroelectric switching and a minority antiferroelectric transition (Figure 1d; Figure S2, Supporting Information), which suggests the phase boundary being located near $x = 0.15$; consistent with the structural evolution (Figure 1a), and in agreement with observations in bulk-ceramic counterparts.[31]

To further illustrate the evolution of the $Pb_{1-x}Ba_xZrO_3$ films, a simple phase diagram is provided (**Figure 2a**), which summarizes the polarization-switching peaks including the antiferroelectric-to-ferroelectric transition fields ($\pm E_{A\text{-}F}$) and the ferroelectric-to-antiferroelectric back transition fields ($\pm E_{F\text{-}A}$) for the $x \leq 0.15$ films, as well as the coercive fields ($\pm E_C$) for the ferroelectric-polarization switching for the $x > 0.15$ films. The field values systematically reduce with increasing x; a trend which is ascribed to two factors. First, in the antiferroelectric regime with $x \leq 0.15$, the introduction of barium weakens the stability of the antiferroelectric phase. This can be understood by considering the tolerance factor (t) for ABO_3 perovskites calculated as $t = (r_A+r_O)/[\sqrt{2}(r_B+r_O)]$, where r_A, r_B, and r_O are the radius of the A, B, and oxygen ions, respectively.[32] The ABO_3 structure maintains a nearly ideal cubic configuration when $t \approx 1$ (e.g., $SrTiO_3$). For $t < 1$ (i.e., with decreased r_A and/or increased r_B) the structure tends to stabilize an antiferrodistortive mode (i.e., oxygen-octahedral tilting/rotation) and antiferroelectric phases (e.g., $PbZrO_3$ with $t \approx 0.97$), while for $t > 1$ the structure tends to stabilize a ferrodistortive mode (i.e., ion displacement) and thus ferroelectric phases (e.g., $PbTiO_3$ with $t \approx 1.02$).[33] In the $Pb_{1-x}Ba_xZrO_3$ films, introducing the larger Ba^{2+} ($r = 1.35$ Å) to partially replace Pb^{2+} ($r = 1.20$ Å) increases the average r_A and t, destabilizing the antiferroelectric phase and therefore reducing the antiferroelectric-to-ferroelectric transition fields (both $E_{A\text{-}F}$ and $E_{F\text{-}A}$), until the material fully evolves into a ferroelectric for $x > 0.15$. Second, in the ferroelectric regime with x further increasing toward 0.45, the coercive field E_C continues to decrease (from ≈100 to ≈20 kV cm^{-1}), accompanied by a remarkably suppressed polarization hysteresis (Figure 1e–g). This demonstrates another effect of barium incorporation, that is, the introduction of relaxor-like features. To explore this point further, the temperature-dependent dielectric responses of parent-$PbZrO_3$ films (Figure 2b) are compared to those of the representative $Pb_{0.85}Ba_{0.15}ZrO_3$ (Figure S3, Supporting Information) and $Pb_{0.65}Ba_{0.35}ZrO_3$ (Figure 2c) films, all measured with pristine, unpoled capacitors. The $PbZrO_3$ films exhibit dielectric constant values of ≈220 at 25 °C (with minimal frequency dependence) and a typical antiferroelectric-to-paraelectric phase transition (with the dielectric constant peaking at ≈280 °C), agreeing well with previous reports.[34,35] In contrast, the $Pb_{0.65}Ba_{0.35}ZrO_3$ films exhibit greatly enhanced dielectric constants of ≈1600 at 25 °C (at 2 kHz)

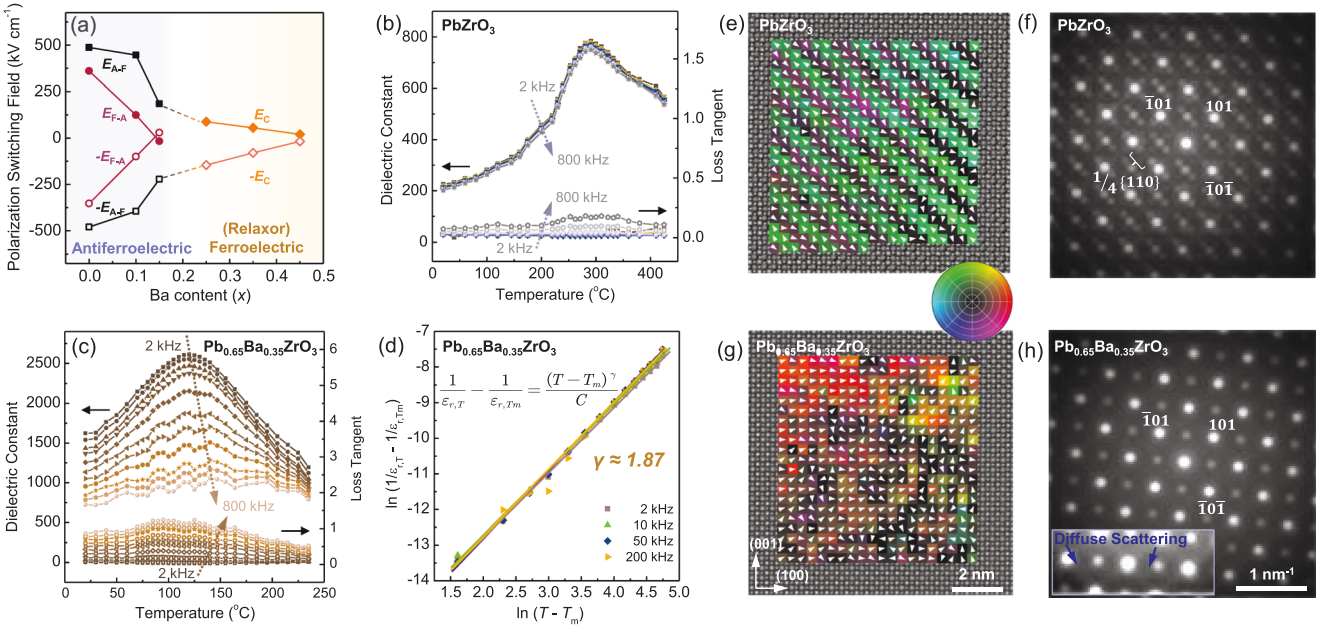

Figure 2. a) Schematic diagram of the antiferroelectric-(relaxor) ferroelectric phase transition. The evolution of the antiferroelectric-to-ferroelectric transition field ($\pm E_{A\text{-}F}$), the ferroelectric-to-antiferroelectric back transition field ($\pm E_{F\text{-}A}$) for $x \leq 0.15$, as well as the coercive field ($\pm E_C$) of ferroelectric polarization switching for $x > 0.15$ are plotted. Temperature-dependent dielectric constant and loss of the $Pb_{1-x}Ba_xZrO_3$ heterostructures with (b) $x = 0.0$ and (c) $x = 0.35$. d) Fits of the temperature (T)-dependent dielectric constant data for $x = 0.35$ heterostructures based on the modified Curie-Weiss law. $\varepsilon_{r,T}$ is the dielectric constant at T, which reaches the maximum $\varepsilon_{r,Tm}$ at the temperature T_m. C is a constant. e) Atomic-resolution iDPC image with projected local polar displacements of the $PbZrO_3$ ($x = 0$) films. The color map represents both the direction and the magnitude (ranging from 0 to 35 pm) of the displacements. f) Averaged NBED pattern over a few hundred of nanometers in the $PbZrO_3$ ($x = 0$) films. The diffraction intensity is on a logarithmic scale. g) Atomic-resolution iDPC image with projected local polar displacements of the $Pb_{0.65}Ba_{0.35}ZrO_3$ ($x = 0.35$) films. The color map represents both the direction and the magnitude (ranging from 0 to 10 pm) of the displacements. h) Averaged NBED pattern of the $Pb_{0.65}Ba_{0.35}ZrO_3$ ($x = 0.35$) films. The amplified inset with higher contrast highlights the diffuse scattering.

with a noticeable frequency dependence. The peaks in the dielectric constant versus temperature curves (denoted as T_m) become diffuse and are lowered to ≈120 °C (at 2 kHz). Moreover, the T_m values show a frequency dispersion of ≈20 °C upon evolving from 2 kHz to 800 kHz, Figure 2c); which indicates a key relaxor feature of the $Pb_{0.65}Ba_{0.35}ZrO_3$ films.[36,37] Using the modified Curie-Weiss law,[15] the temperature-dependent dielectric constant data were fitted to provide a quantitative evaluation of the relaxor nature. The relaxor diffuseness coefficient γ in the modified Curie-Weiss law is found to be ≈ 1.23 for the $PbZrO_3$ films [close to the value for an ideal (anti)ferroelectric (with $\gamma \approx 1.0$)], ≈ 1.48 for the $Pb_{0.85}Ba_{0.15}ZrO_3$ films, and ≈ 1.87 for the $Pb_{0.65}Ba_{0.35}ZrO_3$ films [close to the value for an ideal relaxor (with $\gamma \approx 2.0$)], indicating enhanced relaxor features in the $Pb_{1-x}Ba_xZrO_3$ films with increased barium content (Figure 2d; Figure S3, Supporting Information).

To understand the microscopic structural evolution and the atomic origin of such relaxor nature, scanning transmission electron microscopy studies were conducted on the $Pb_{0.65}Ba_{0.35}ZrO_3$ films in comparison to the parent $PbZrO_3$ films (Experimental Section). Atomic-resolution integrated differential phase contrast (iDPC) images of the $PbZrO_3$ films (Figure 2e) indicate key antiferroelectric characteristics with antiparallel order of local dipoles (with cation displacements in a ↑↑↓↓ pattern) along the $<110>_{pc}$.[21,30] Such polar order quadruples the unit cell and gives rise to well-resolved $1/4\{110\}_{pc}$ superlattice reflections in nanobeam diffraction (NBED) patterns (Figure 2f, which is the averaged pattern over a few hundred of nanometers). These features of antiferroelectricity are, however, absent in the $Pb_{0.65}Ba_{0.35}ZrO_3$ films, which instead display highly disordered local dipoles with reduced magnitude (Figure 2 g), resembling slush-like polar structures (multi-nanodomain state with a high density of low-angle domain walls) that are typically observed in relaxors.[38] As a result, the NBED patterns of the $Pb_{0.65}Ba_{0.35}ZrO_3$ films (Figure 2 h) exhibit no superlattice reflections but instead show "butterfly"-shaped diffuse scattering along the $<110>_{pc}$; another signature of the slush-like polar nanodomains in relaxors.[38,39] These pronounced relaxor features in the $Pb_{0.65}Ba_{0.35}ZrO_3$ films are likely attributed to the substantial enhancement of local chemical and structural heterogeneities resulting from the substitution of Ba^{2+} into the Pb^{2+} sites, which disrupts the long-range (anti-)ferroelectric order in $Pb_{1-x}Ba_xZrO_3$, and leads to the formation of short-range-ordered polar nanodomains (Figure 2 g), akin to the structural evolutions observed in prototypical ferroelectric-based relaxors.[40,41]

Having realized relaxor features from this antiferroelectric-based system, attention is now turned to exploring the potential of the materials as tunable dielectrics, wherein the dielectric constant should be readily adjusted with external voltages (electric fields).[42] The field-dependent dielectric response of the $Pb_{1-x}Ba_xZrO_3$ films was measured first at low frequency (10 kHz), in the form of out-of-plane-oriented, parallel-plate capacitors (with $SrRuO_3$ as top and bottom electrodes, with an AC excitation field of 2 kV cm^{-1}, and at room

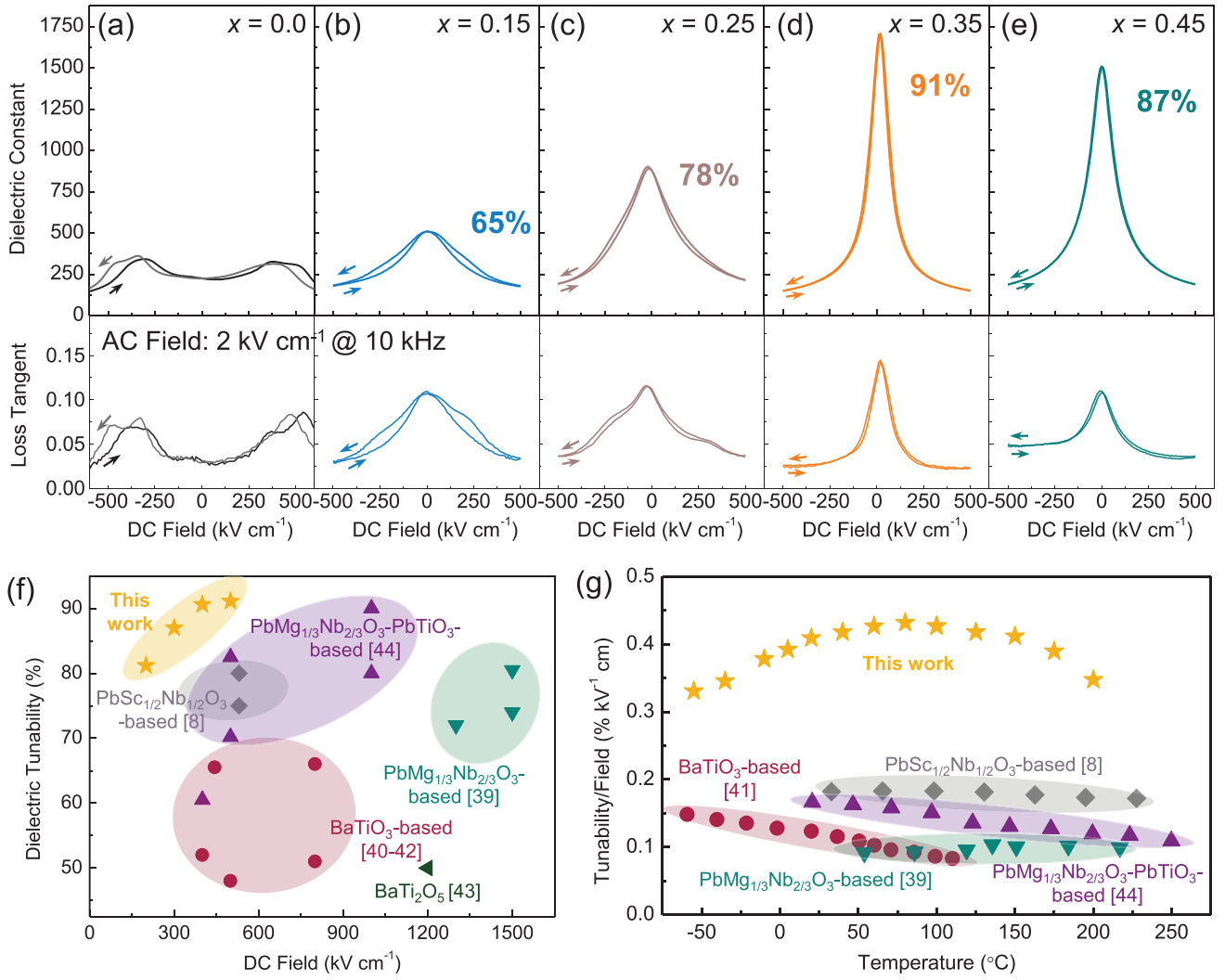

Figure 3. Dielectric constant and loss of the $Pb_{1-x}Ba_xZrO_3$ heterostructures with (a) $x = 0.0$ (pure $PbZrO_3$), b) $x = 0.15$, c) $x = 0.25$, d) $x = 0.35$, and (e) $x = 0.45$ as a function of DC bias field, measured with an AC excitation field of 2 kV cm^{-1} and at a frequency of 10 kHz. The dielectric tunability values (in percentage) are calculated as the change of the dielectric constant with the bias field increasing from 0 to ±500 kV cm^{-1}. f) Comparison of the dielectric tunability values and applied DC bias fields of the $Pb_{1-x}Ba_xZrO_3$ heterostructures (measured at 10 kHz) in this work and other typical tunable-dielectric films (measured across the 1–100 kHz frequency range) in the literature.[8,43–48] g) Comparison of the tunability/field ratios and measurement temperatures of the $Pb_{0.65}Ba_{0.35}ZrO_3$ heterostructures in this work and other typical tunable-dielectric films in the literature.[8,43,45,48]

temperature of 20 °C; **Figures** 3a–e). The antiferroelectric $PbZrO_3$ films (Figure 3a) exhibit a "positive" dielectric tunability as previously reported (i.e., the dielectric constant increases with increasing DC bias field),[18] which peaks (with tunability values of ≈ 50%) at the antiferroelectric-to-ferroelectric transition fields (400–500 kV cm^{-1}; with peaks in the loss curves at similar fields). Upon crossing over to the (relaxor) ferroelectric materials (for $x \geq 0.15$), the dielectric tunability transforms from "positive" to "negative" (i.e., the dielectric constant decreases with increasing DC bias field) as a result of the gradual polarization saturation. For the $x = 0.15$ films (Figure 3b), both the dielectric constant and loss curves exhibit shoulders to the main peaks corresponding to the residual antiferroelectric phase, in agreement with the polarization switching behavior (Figure 1d). As x is further increased, the relaxor phase becomes dominant and the hysteresis in the dielectric curves becomes negligible, which contributes to enhanced dielectric tunability, reaching ≈78%, ≈91%, and ≈87% at a DC bias field of 500 kV cm^{-1} for films with $x = 0.25$ (Figure 3c), 0.35 (Figure 3d), and 0.45 (Figure 3e), respectively. Such exceptionally high dielectric tunability values achieved in the $Pb_{1-x}Ba_xZrO_3$ films, particularly at comparatively lower electric fields (e.g., 81% tunability at merely 200 kV cm^{-1} for the $Pb_{0.65}Ba_{0.35}ZrO_3$ films), position them as superior in terms of responsiveness when compared to the parent $PbZrO_3$ antiferroelectric films, prototypical relaxor films such as $PbMg_{1/3}Nb_{2/3}O_3$ and $PbSc_{1/2}Nb_{1/2}O_3$,[8,43,44] as well as relaxor films derived from ferroelectrics such as $BaTiO_3$-based and (1-x)$PbMg_{1/3}Nb_{2/3}O_3$-(x)$PbTiO_3$-based materials (Figure 3f),[45–48] providing new potential candidates for highly-sensitive varactors (variable capacitors) and sensors.

It is proposed that the outstanding performance of the $Pb_{1-x}Ba_xZrO_3$ films, as compared with traditional relaxors derived from ferroelectrics, can be attributed to their complex phase evolution that leads to unconventional relaxor nature (Figure 2d). Traditional relaxors derived from ferroelectrics gain their intriguing properties as the result of the competition between two phases (i.e., ferroelectric and paraelectric),[10] leading to the formation of polar nanodomains at the expense of the (uniform) polar phase, and consequently, they exhibit suppressed polarizability/permittivity with (somewhat) limited tunability.[49] In contrast, the $Pb_{1-x}Ba_xZrO_3$ films experience a more complex phase evolution with multi-phase competition among antiferroelectric, ferroelectric, and paraelectric order. This complex interplay introduces enhanced local heterogeneities that disrupt the long-range polar order, fragmenting it into slush-like nanodomains while preserving a substantial proportion of the polar phases (Figure 2g). Superior responsiveness is thus achieved in the $Pb_{1-x}Ba_xZrO_3$ relaxor films, with the dielectric constant (and its tunability) being a signature manifestation. For the best-performing $Pb_{0.65}Ba_{0.35}ZrO_3$ composition, the highly responsive slush-like nanodomains (Figure 2g) contribute to an ultrahigh dielectric constant >1600 even in just 100-nm-thick films (Figure 2c); a value which is five times higher than the dielectric constant (200-300) of $Ba_{1-x}Sr_xTiO_3$ films of the same thickness.[49] Under a relatively low bias field, these nanodomains in $Pb_{0.65}Ba_{0.35}ZrO_3$ could be readily manipulated and poled (Figure 1f), thus their contribution to the dielectric response becomes almost frozen (with only electronic and ionic polarization remaining active), leading to a substantial decrease of the relative permittivity (thus a high dielectric tunability) and simultaneously reduced dielectric loss (e.g., from ≈0.13 at zero field to ≈0.02 at 500 kV cm^{-1}; Figure 3a-e). Moreover, the $Pb_{0.65}Ba_{0.35}ZrO_3$ films exhibit good thermal stability due to the more diffuse relaxor-phase transition, which, across a broad temperature range from -55 to 200 °C, ensures a high tunability (>65% at 200 kV cm^{-1}; Figure S4, Supporting Information) and an impressive tunability/field ratio >0.3 kV^{-1}•cm•% (more than twice of the values from conventional relaxor films; Figure 3g),[8,43,45,48] highlighting their potential to sustain high responsiveness across a wide variety of scenarios.

Having demonstrated the high responsiveness and tunability of the $Pb_{1-x}Ba_xZrO_3$ relaxor films in the quasi-static frequency (~kHz) range, the highest-performing films (i.e., $Pb_{0.65}Ba_{0.35}ZrO_3$) were down-selected for further capacitance measurements in the 0.1-20 GHz range to evaluate their practical applicability as microwave-tunable dielectrics. For such measurements, the parallel-plate capacitors used for the low-frequency study are no longer adequate because the $SrRuO_3$ electrodes considerably degrade in conductivity in the GHz range. On the other hand, parallel-plate capacitors with metal electrodes (which are neither structurally or lattice compatible with the oxide layers) preclude the synthesis of high-quality $Pb_{0.65}Ba_{0.35}ZrO_3$ films. Instead, coplanar-geometry gold interdigital capacitors (IDCs) were utilized for the high-frequency studies,[6] and fabricated on the surface of the 100-nm-thick $Pb_{0.65}Ba_{0.35}ZrO_3$ films that were grown coherently on 60-nm $BaZrO_3$-buffered $(LaAlO_3)_{0.3}(Sr_2AlTaO_6)_{0.7}$ (LSAT) $(001)_{pc}$ substrates (Experimental Section and Figure S5, Supporting Information). The $BaZrO_3$/LSAT $(001)_{pc}$ substrates are specifically chosen due to the fact that they are (essentially) field-insensitive linear dielectrics with low dielectric constant (≈40 for $BaZrO_3$ and ≈22 for LSAT) and low loss (<0.01); therefore, providing an ideal platform for the study of $Pb_{0.65}Ba_{0.35}ZrO_3$ relaxor films. The IDC capacitance of the $Pb_{0.65}Ba_{0.35}ZrO_3$/$BaZrO_3$/LSAT $(001)_{pc}$ heterostructures was tested and mapped over a bias-field range of ±667 kV cm^{-1} and a frequency range of 0.1–20 GHz (**Figure 4a**). The 2D map in frequency and field space demonstrates the high dielectric tunability preserved in the heterostructures at these higher frequencies (e.g., ≈56% under 600 kV cm^{-1} at 1 GHz). Parallel measurements on the bare $BaZrO_3$/LSAT $(001)_{pc}$ substrates with IDCs of the same geometry reveal a constant capacitance with negligible field dependence (Figure 4b), confirming that the tunability of the $Pb_{0.65}Ba_{0.35}ZrO_3$/$BaZrO_3$/LSAT $(001)_{pc}$ heterostructures arises solely from the $Pb_{0.65}Ba_{0.35}ZrO_3$ layer. It is expected that the tunability can be further enhanced by thinning down the inactive substrate. Nevertheless, the tunability of the current heterostructures outperform that of typical microwave-dielectric films, especially at relatively low fields (Figure 4c). For example, at 1 GHz the $Pb_{0.65}Ba_{0.35}ZrO_3$ heterostructures achieve a tunability of ~37% under a bias field of 100 kV cm^{-1}, which is higher than the tunability of the 5($SrTiO_3$)-($BaTiO_3$)-SrO films [7] and the $Ba_{1-x}Sr_xTiO_3$ films [50] at the same field. It is noted that the $Pb_{0.65}Ba_{0.35}ZrO_3$ heterostructures have a frequency dependence, where both the IDC capacitance (Figures 4a) and the dielectric tunability reduce with increasing frequency (Figures 4a,b; Figure S6, Supporting Information), likely because the polar structures become less responsive at higher frequencies.

The $Pb_{0.65}Ba_{0.35}ZrO_3$ heterostructures also exhibit a frequency- and field-dependence of the quality factor $Q(E)$ (i.e., the inverse of the loss tangent, Figures 4d). The quality factor is relatively low (<10) at zero field, yet increases to the level of 10^2–10^3 at a bias field of 200–600 kV cm^{-1} over the range of 0.5–10 GHz; comparable with that of typical $Ba_{1-x}Sr_xTiO_3$ tunable dielectric films (Figures 4e,f). The quality factor also shows a complex frequency-field coupling that resonates at specific frequency-field combinations, reaching peak values exceeding 10^3. Such field-dependent frequency resonances were also reported before in strain-engineered $Ba_{1-x}Sr_xTiO_3$ films (thickness ≈ 100 nm), and were ascribed to reversible domain-wall oscillation in high-density nanoscale domains.[6,51] Similar effects should be possible in this case in the $Pb_{0.65}Ba_{0.35}ZrO_3$ relaxor films with slush-like nanodomain structures (Figure 2g). Furthermore, the commutation quality factor CQF = $(\varepsilon_{r,0} - \varepsilon_{r,E})^2/(\varepsilon_{r,0}\bullet\varepsilon_{r,E})\bullet Q(E=0)\bullet Q(E)$, which incorporates the dielectric tunability and loss properties under both zero and bias fields, and is a key figure of merit for radio-frequency tunable dielectrics, was calculated.[7] With the preserved high tunability and the resonance-induced high quality factor (low loss) at specific radio frequencies, the $Pb_{0.65}Ba_{0.35}ZrO_3$ heterostructures can realize large CQF values (e.g., >2000 at 1 GHz and with peak values reaching 10^4 at 600 kV cm^{-1}; Figure S7, Supplementary Information); comparable to, if not better than, typical $Ba_{1-x}Sr_xTiO_3$ and 5($SrTiO_3$)-($BaTiO_3$)-SrO microwave dielectrics (Table S3, Supplementary Information).[7,50] This high performance places the $Pb_{0.65}Ba_{0.35}ZrO_3$ relaxor films in a competitive position for the practical application of tunable dielectrics in radio-frequency electronics including phase shifters, tunable filters, resonators, and beyond.

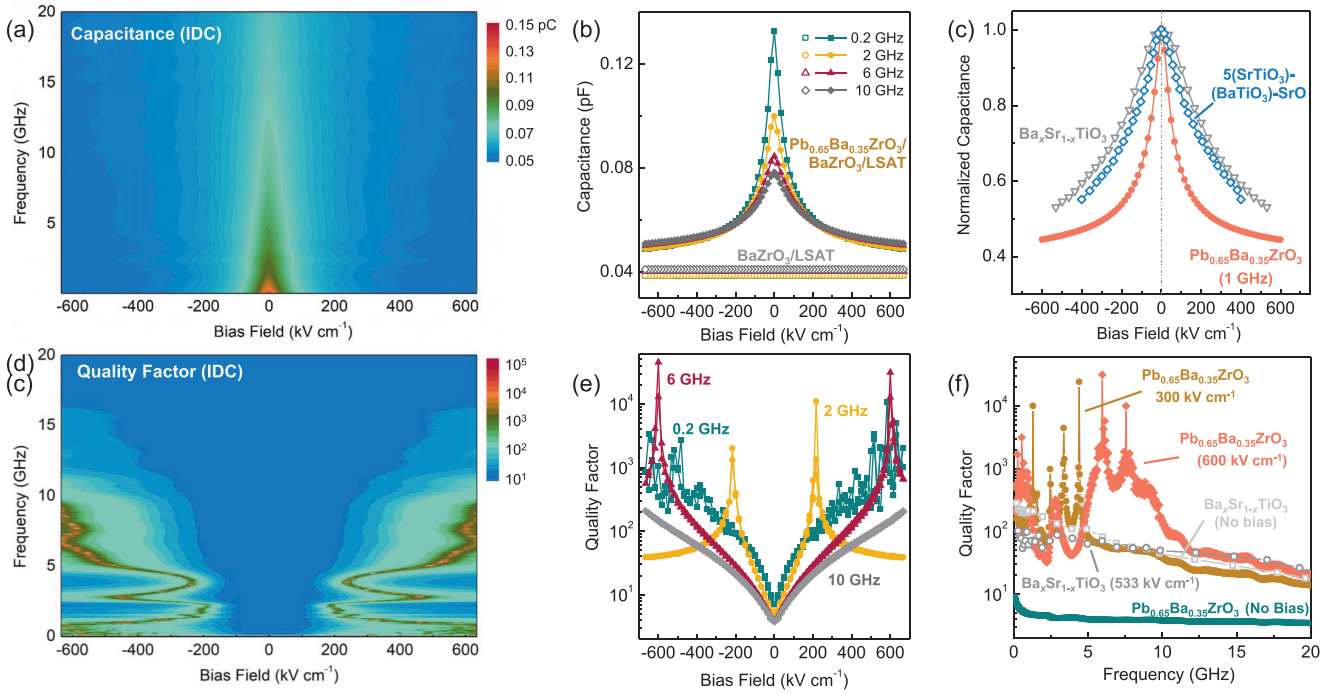

Figure 4. a) Mapping of the radio-frequency capacitance of the IDCs on the $Pb_{0.65}Ba_{0.35}ZrO_3$/$BaZrO_3$/LSAT (001) heterostructures over a bias-field range of ±667 kV cm^{-1} and a frequency range of 0.1–20 GHz. b) Comparison of the field-dependent capacitance values (at selected frequencies) of the IDCs on the $Pb_{0.65}Ba_{0.35}ZrO_3$/$BaZrO_3$/LSAT $(001)_c$ heterostructures and on the $BaZrO_3$/LSAT substrates. c) Comparison of the field-dependent radio-frequency capacitance values of the $Pb_{0.65}Ba_{0.35}ZrO_3$ heterostructures and those of the typical tunable dielectrics including typical $Ba_{1-x}Sr_xTiO_3$ films[50] and the 5($SrTiO_3$)-($BaTiO_3$)-SrO films.[7] d) Mapping of the quality factor of the IDCs on the $Pb_{0.65}Ba_{0.35}ZrO_3$/$BaZrO_3$/LSAT (001) heterostructures over the same field and frequency ranges as in (a). e) Field-dependent quality factor of the IDCs on the $Pb_{0.65}Ba_{0.35}ZrO_3$/$BaZrO_3$/LSAT $(001)_c$ heterostructure at selected radio-frequencies. f) Frequency-dependence of the quality factor values of the $Pb_{0.65}Ba_{0.35}ZrO_3$/$BaZrO_3$/LSAT (001) heterostructures at various bias fields of 0, 300, and 600 kV cm^{-1}. The quality factor values of typical $Ba_{1-x}Sr_xTiO_3$ films[50] at bias fields of 0 and 533 kV cm^{-1} are also presented for comparison.

3. Conclusion

This work demonstrates the feasibility and efficacy of developing new relaxors from antiferroelectric materials and showcases their potential for use in tunable dielectrics with ultrahigh responsiveness. By alloying the archetypal antiferroelectric $PbZrO_3$ with the dielectric $BaZrO_3$, relaxor features are achieved with a complex phase evolution and an unconventional multi-phase competition among antiferroelectric, ferroelectric, and paraelectric order. This complex interplay greatly enhances the local heterogeneities and results in relaxor characteristics while preserving a considerable polar nature. Consequently, the $Pb_{0.65}Ba_{0.35}ZrO_3$ films achieve ultrahigh dielectric tunability values under low bias fields (≈81% at 200 kV cm^{-1} and ≈91% at 500 kV cm^{-1}) at 10 kHz, outcompeting most traditional relaxor-ferroelectric films. The high tunability is sustained in the radio-frequency (0.1–20 GHz) range and is coupled with a large commutation quality factors (>10^3). These findings shed light on the phase evolution process between antiferroelectrics and relaxors, highlighting a promising pathway to develop relaxor materials with exceptional performance by constructing complex multi-phase competition and slush-like highly responsive local polar structures. This approach should be generally applicable to other material systems (e.g., the lead-free $NaNbO_3$ and $AgNbO_3$ antiferroelectrics), compositions (e.g., solid solutions combining starting materials with antiferroelectric, ferroelectric, and paraelectric order, respectively), and other forms (e.g., polycrystalline films or bulk ceramics), so as to provide new possibilities for enhanced functionalities in various applications (pyroelectrics, electrocalorics, pulsed-power capacitors, etc.) where agile property tunability is required.

4. Experimental Section

Film Growth: 45 nm $SrRuO_3$ / 100 nm $Pb_{1-x}Ba_xZrO_3$ (x = 0-0.45) / 30 nm $SrRuO_3$ / $DyScO_3$ $(110)_O$ (Crystec, GmbH) and 100 nm $Pb_{0.65}Ba_{0.35}ZrO_3$ / 60 nm $BaZrO_3$ / LSAT $(001)_c$ (MTI Corp.) thin-film heterostructures were synthesized via pulsed-laser deposition using a KrF excimer laser (248 nm, LPX 300, Coherent) in an on-axis growth geometry. Growth of the heterostructures was completed from ceramic targets of composition $SrRuO_3$, $PbZrO_3$, and $BaZrO_3$ (Praxair Inc., with purity >99.9%) with a target-to-substrate distance of ≈55 mm. The targets were sanded, cleaned, and sufficiently pre-ablated prior to each growth. For the $SrRuO_3$/$Pb_{1-x}Ba_xZrO_3$/$SrRuO_3$/$DyScO_3$ $(110)_O$ heterostructures, the bottom electrode $SrRuO_3$ was deposited at a heater temperature of 700 °C (as measured by a thermocouple in the heater block) in a dynamic oxygen pressure of 100 mTorr, at a laser fluence of ≈1.4 J cm^{-2}, and at a laser repetition rate of 15 Hz. The $Pb_{1-x}Ba_xZrO_3$ layers were grown by alternate laser ablation on the $PbZrO_3$ and $BaZrO_3$ ceramic targets, during which the pulse numbers on each target was programmed in each cycle to control the overall $Pb_{1-x}Ba_xZrO_3$ composition (Table S1, Supporting Information). The growth was conducted at a heater temperature of 600 °C in a dynamic oxygen pressure of 80 mTorr, at a laser fluence of

≈1.3 J cm^{-2}, and at a laser repetition rate of 5 Hz. Finally, the top electrode $SrRuO_3$ was deposited in situ after the $Pb_{1-x}Ba_xZrO_3$ growth with the same growth parameters as the bottom $SrRuO_3$ layer, but at a lower heater temperature of 550 °C to reduce the (potential) volatilization of lead from the $Pb_{1-x}Ba_xZrO_3$ layer. For the $Pb_{0.65}Ba_{0.35}ZrO_3/BaZrO_3$/LSAT $(001)_c$ heterostructures, the $BaZrO_3$ buffer layer was deposited at a heater temperature of 700 °C in a dynamic oxygen pressure of 20 mTorr, at a laser fluence of ≈2.2 J cm^{-2}, and a laser repetition rate of 5 Hz. The subsequent $Pb_{0.65}Ba_{0.35}ZrO_3$ layer was deposited with the same parameters as noted above for the $Pb_{1-x}Ba_xZrO_3$ layers. After all depositions, the heterostructures were cooled to room temperature at a rate of 10 °C min^{-1} in a static oxygen pressure of ≈700 Torr.

Structural Characterization: X-ray line scans and reciprocal space mapping studies of the heterostructures were conducted with a high-resolution X-ray diffractometer (copper source, $K_{\alpha 1}$ radiation of a wavelength of 1.5406 Å; Panalytical, X'pert^3 MRD), using a hybrid two-bounce primary monochromator to generate the incident X-ray beam and a PIXcel3D position-sensitive detector. The line scans were performed in a symmetric set-up with a 1/2° receiving slit and a point detector. The scanning speed was 0.01° and 0.5 s per step. The reciprocal space maps were obtained in an asymmetric set-up about the 332_O-diffraction condition of the $DyScO_3$ substrate, with a 1/16° receiving slit and a line detector (with an active length of 2.51° in the 2θ angle). The scanning speed was 0.01° (in omega angle) and 4 s per step.

Scanning Transmission Electron Microscopy (STEM): STEM samples were prepared using a focused-ion beam following standard lift-out procedures.[52] The samples were thinned to electron transparency with the gallium beam energy decreasing from 30 to 5 kV. Final thinning to remove the damage was performed using broad-beam argon ion milling (Fischione 1051 TEM Mill) with beam energies of 0.3 and 0.1 kV. For STEM, a probe aberration-corrected Thermo Fisher Scientific Themis-Z S/TEM was operated at 200 kV. Nanobeam electron diffraction patterns were collected with an electron microscope pixel array detector at a dwell time of 1 µs and a semi-convergence angle of ≈0.6 mrad.[53] Twenty frames of atomic-resolution annular dark field and iDPC images were simultaneously acquired with a 1-µs dwell time, then registered and averaged to improve the signal-to-noise ratio and minimize spatial drift. Atomic columns were fitted using a 2D Gaussian function, and projected polar displacements were calculated from the relative shift between the center of mass of cations (lead and zirconium) with respect to the surrounding anions (oxygen).

Low-frequency Electrical Measurements: Capacitor structures are fabricated via photolithography and etching for the electrical measurements of the $SrRuO_3/Pb_{1-x}Ba_xZrO_3/SrRuO_3/DyScO_3$ (110) heterostructures. To do this, an OCG 825 (G-line positive) photoresist layer was spin-coated on the heterostructures, exposed under a photoresist mask, and then developed and patterned into arrays of circles with diameters of 50 µm. The top $SrRuO_3$ layer was then selectively etched by either a $NaIO_4$ aqueous solution (0.1 mol l^{-1}) or ion milling to realize circular capacitor structures. Polarization-electric-field hysteresis loops were then measured with a bipolar triangular voltage profile at a frequency of 10 kHz using a Precision Multiferroic Tester (Radiant Technologies). Dielectric constant data for the heterostructures as a function of frequency (2–800 kHz), DC bias field (up to ±500 kV cm^{-1}), and temperature (20–420 °C) were obtained using an impedance analyzer (E4990A, Keysight Technologies) with an excitation AC field of 2 kV cm^{-1}. The temperature of the samples was controlled by a customized heater (Neocera LLC) during measurement.

Radio-Frequency IDC Device Fabrication: Two-port IDC electrodes with a finger spacing of 3 µm were fabricated on the $Pb_{0.65}Ba_{0.35}ZrO_3/BaZrO_3$/LSAT $(001)_c$ heterostructures using a lift-off metallization process. A schematic structure of the IDC electrodes is shown (Figure S5, Supporting Information). To begin, the samples were cleaned with ultrasonic agitation in acetone, followed by an isopropanol rinse. The resist stack consisted of 2.2 µm of polydimethylglutarimide (PMGI) polymer topped by 1.8 µm of negative photoresist (AZ nLOF-2020). The PMGI was baked for 5 min at 180 °C and then cooled to 50 °C at 5 °C min^{-1} before the imaging resist was spun, then baked at 110 °C and similarly cooled. The negative imaging resist was exposed through a photomask using projection lithography and developed in tetra-methyl ammonium hydroxide developer. After rinsing in deionized water, the sample was flood-exposed with deep ultraviolet light to scissor the cross-linked PMGI underlayer. The ultraviolet-scissored PMGI underlayer was developed using a tetra-ethyl ammonium hydroxide developer, in which the imaging resist is insoluble, yielding a retrograde profile in the resist sidewall. Finally, 15 nm of titanium was evaporated by electron-beam evaporation as an adhesion layer, followed by 1 µm of gold. The sample was then soaked in 1165 solvent overnight to complete the lift-off.

Microwave Radio-Frequency Dielectric Measurements: Devices were tested using a two-port microwave setup capable of applying large DC bias voltage (Figure S5, Supporting Information). Data were collected for the frequency and voltage dependence of the two-port complex reflection coefficients from 0.1 GHz to 20 GHz in 100-MHz steps and for an applied bias range from −200 V to +200 V (corresponding to $|\boldsymbol{E}| \leq 0.67$ MV cm^{-1}) along the $[100]_{pc}$ orientation. Microwave radio-frequency measurements were performed using a two-port programmable vector network analyzer (VNA; Agilent N5222B, 26.5 GHz) and a MPI TS150 probe station equipped with 150-µm coplanar ground–signal–ground probes (Infinity I40-A-150-GSG-HC, FormFactor). The system was cabled with flexible radio-frequency cables fitted with 2.92-mm K-connectors. External high-voltage bias tees (SHF BT45R-B) attached in-line at the probe heads allowed a DC bias voltage, supplied by an external Keithley 2612A source-measurement unit, to be applied to the IDC electrodes during the radio-frequency measurements of the frequency and voltage dependence of the two-port complex reflection coefficients. The measurement system was calibrated using a line-reflect-reflect-match algorithm. The calibration measurements were performed with WinCal XE software from Cascade Microtech using thru, short, and 50-Ω-load standards on an impedance standard substrate (104-783, FormFactor) and an open load standard formed by raising the probe station platen lever to lift the probes to more than 200 µm above the impedance-standard substrate. Each frequency sweep was composed of three averaged sweeps with a system (intermediate frequency) bandwidth of 200 Hz, corresponding to a noise floor better than −100 dBm. The VNA power level was set to −15 dBm with a power slope of 0.1 dB GHz^{-1} to compensate for increased cable loss at higher frequencies. When collecting the data, voltage was stepped from zero to 5 V, to −5 V, to 10 V, to −10 V, and so on, to ±200 V. At each bias point, the voltage was held until the three sweeps needed for averaging were completed. After collecting the data for each bias point the voltage was changed and the averaging was reset to ensure no carry over of data from the previous bias set point. The total applied voltage was divided across the two device ports, referenced to port 1 so that for a given bias V, V/2 was applied to port 1 and −V/2 was applied to port 2, with polarities inverted for negative bias points.

Supporting Information

Supporting Information is available from the Wiley Online Library or from the author.

Acknowledgements

The auhtors thank Dr. Jaegyu Kim for helpful discussions. H.P., L.W., D.W., K.C., B.H., J.E.S., and L.W.M. acknowledge that research was sponsored by the Army Research Laboratory and was accomplished under Cooperative Agreement Number W911NF-24-2-0100. The views and conclusions contained in this document are those of the authors and should not be interpreted as representing the official policies, either expressed or implied, of the Army Research Laboratory or the U.S. Government. The U.S. Government is authorized to reproduce and distribute reprints for Government purposes notwithstanding any copyright notation herein. Z.T. acknowledges support from the Air Force Office of Scientific Research under award number FA9550-24-1-0266. Any opinions, findings, and conclusions or recommendations expressed in this material are those of the author(s) and do not necessarily reflect the views of the United States Air Force.

X.H. acknowledges support from the SRC-JUMP ASCENT center. H.Z. acknowledges financial support from the Department of Defense, Air Force Office of Scientific Research under Grant No. FA9550-18-1-0480. S.P. acknowledges the support of the National Science Foundation under Grant DMR-2329111. J.E.S. and L.W.M. acknowledge additional support from the Army Research Office under grant W911NF-21-1-0126.

Conflict of Interest

The authors declare no conflict of interest.

Data Availability Statement

The data that support the findings of this study are available from the corresponding author upon reasonable request.

Keywords

antiferroelectric, dielectric tunability, lead zirconate, radio frequency, relaxor, thin film

Received: March 19, 2025
Revised: May 19, 2025
Published online: May 29, 2025

[1] R. Ramesh, S. Salahuddin, S. Datta, C. H. Diaz, D. E. Nikonov, I. A. Young, D. Ham, M. Chang, W. Khwa, A. S. Lele, C. Binek, Y. Huang, Y. Sun, Y. Chu, B. Prasad, M. Hoffmann, J. Hu, Z. J. Yao, L. Bellaiche, P. Wu, J. Cai, J. Appenzeller, S. Datta, K. Y. Camsari, J. Kwon, J. A. C. Incorvia, I. Asselberghs, F. Ciubotaru, S. Couet, C. Adelmann, et al., *APL Mater.* **2024**, *12*, 99201.
[2] D. E. Nikonov, I. A. Young, *Ieee J. Explor. Solid-State Comput. Devices Circuits* **2015**, *1*, 3.
[3] Y. Jiang, E. Parsonnet, A. Qualls, W. Zhao, S. Susarla, D. Pesquera, A. Dasgupta, M. Acharya, H. Zhang, T. Gosavi, C. C. Lin, D. E. Nikonov, H. Li, I. A. Young, R. Ramesh, L. W. Martin, *Nat. Mater.* **2022**, *21*, 779.
[4] C. Lee, N. D. Orloff, T. Birol, Y. Zhu, V. Goian, E. Rocas, R. Haislmaier, E. Vlahos, J. A. Mundy, L. F. Kourkoutis, Y. Nie, M. D. Biegalski, J. Zhang, M. Bernhagen, N. A. Benedek, Y. Kim, J. D. Brock, R. Uecker, X. X. Xi, V. Gopalan, D. Nuzhnyy, S. Kamba, D. A. Muller, I. Takeuchi, J. C. Booth, C. J. Fennie, D. G. Schlom, *Nature* **2013**, *502*, 532.
[5] S. Gevorgian, *Ferroelectrics in Microwave Device, Circuits and Systems*, Springer, Berlin germany **2009**.
[6] Z. Gu, S. Pandya, A. Samanta, S. Liu, G. Xiao, C. J. G. Meyers, A. R. Damodaran, H. Barak, A. Dasgupta, S. Saremi, A. Polemi, L. Wu, A. A. Podpirka, A. Will-Cole, C. J. Hawley, P. K. Davies, R. A. York, I. Grinberg, L. W. Martin, J. E. Spanier, *Nature* **2018**, *560*, 622.
[7] N. M. Dawley, E. J. Marksz, A. M. Hagerstrom, G. H. Olsen, M. E. Holtz, V. Goian, C. Kadlec, J. Zhang, X. Lu, J. A. Drisko, R. Uecker, S. Ganschow, C. J. Long, J. C. Booth, S. Kamba, C. J. Fennie, D. A. Muller, N. D. Orloff, D. G. Schlom, *Nat. Mater.* **2020**, *19*, 176.
[8] B. Peng, Q. Lu, Y. Wang, J. Li, Q. Zhang, H. Huang, L. Liu, C. Li, L. Zheng, Z. L. Wang, *Research* **2022**, *2022*, 9764976.
[9] A. K. Taganstev, V. O. Sherman, K. F. Astafiev, J. Venkatesh, N. Setter, *J. Electroceram* **2003**, *11*, 5.
[10] L. B. Kong, S. Li, T. S. Zhang, J. W. Zhai, F. Y. C. Boey, J. Ma, *Prog. Mater. Sci.* **2010**, *55*, 840.
[11] L. P. Curecheriu, A. Ianculescu, L. Mitoseriu, *J. Eur. Ceram. Soc.* **2010**, *30*, 599.
[12] V. V. Shvartsman, B. Dkhil, A. L. Kholkin, *Annu. Rev. Mater. Sci.* **2013**, *43*, 423.
[13] H. Pan, F. Li, Y. Liu, Q. Zhang, M. Wang, S. Lan, Y. Zheng, J. Ma, L. Gu, Y. Shen, P. Yu, S. Zhang, L. Chen, Y. Lin, C. Nan, *Science* **2019**, *365*, 578.
[14] F. Li, S. Zhang, Z. Xu, L. Q. Chen, *Adv. Funct. Mater.* **2017**, *27*, 1700310.
[15] H. Pan, S. Lan, S. Xu, Q. Zhang, H. Yao, Y. Liu, F. Meng, E. Guo, L. Gu, D. Yi, X. R. Wang, H. Huang, J. L. MacManus-Driscoll, L. Chen, K. Jin, C. Nan, Y. Lin, *Science* **2021**, *374*, 100.
[16] C. A. Randall, Z. Fan, I. Reaney, L. Q. Chen, S. Trolier-McKinstry, *J. Am. Ceram. Soc.* **2021**, *104*, 3775.
[17] X. Tan, C. Ma, J. Frederick, S. Beckman, K. G. Webber, *J. Am. Ceram. Soc.* **2011**, *94*, 4091.
[18] H. Pan, Z. Tian, M. Acharya, X. Huang, P. Kavle, H. Zhang, L. Wu, D. Chen, J. Carroll, R. Scales, C. J. G. Meyers, K. Coleman, B. Hanrahan, J. E. Spanier, L. W. Martin, *Adv. Mater.* **2023**, *35*, 2300257.
[19] C. Liu, Y. Si, H. Zhang, C. Wu, S. Deng, Y. Dong, Y. Li, M. Zhuo, N. Fan, B. Xu, P. Lu, L. Zhang, X. Lin, X. Liu, J. Yang, Z. Luo, S. Das, L. Bellaiche, Y. Chen, Z. Chen, *Science* **2023**, *382*, 1265.
[20] Y. Si, T. Zhang, C. Liu, S. Das, B. Xu, R. G. Burkovsky, X. Wei, Z. Chen, *Prog. Mater. Sci.* **2024**, *142*, 101231.
[21] P. Dufour, T. Maroutian, M. Vallet, K. Patel, A. Chanthbouala, C. Jacquemont, L. Yedra, V. Humbert, F. Godel, B. Xu, S. Prosandeev, L. Bellaiche, M. Otoničar, S. Fusil, B. Dkhil, V. Garcia, *Appl. Phys. Rev.* **2023**, *10*, 21405.
[22] Y. Luo, C. Wang, C. Chen, Y. Gao, F. Sun, C. Li, X. Yin, C. Luo, U. Kentsch, X. Cai, M. Bai, Z. Fan, M. Qin, M. Zeng, J. Dai, G. Zhou, X. Lu, X. Lou, S. Zhou, X. Gao, D. Chen, J. Liu, *Appl. Phys. Rev.* **2023**, *10*, 11403.
[23] Z. Liu, T. Lu, F. Xue, H. Nie, R. Withers, A. Studer, F. Kremer, N. Narayanan, X. Dong, D. Yu, L. Chen, Y. Liu, G. Wang, *Sci. Adv.* **2020**, *6*, aba367.
[24] M. F. Tsai, Y. Z. Zheng, S. C. Lu, J. D. Zheng, H. Pan, C. G. Duan, P. Yu, R. Huang, Y. H. Chu, *Adv. Funct. Mater.* **2021**, *31*, 2105060.
[25] M. Zhang, H. Ding, S. Egert, C. Zhao, L. Villa, L. Fulanović, P. B. Groszewicz, G. Buntkowsky, H. Kleebe, K. Albe, A. Klein, J. Koruza, *Nat. Commun.* **2023**, *14*, 1525.
[26] P. Ge, B. Tian, Z. Hong, M. Liu, S. Yang, X. Ke, *Acta Mater.* **2025**, *286*, 120759.
[27] L. He, Y. Yang, C. Liu, Y. Ji, X. Lou, L. Zhang, X. Ren, *Acta Mater.* **2023**, *249*, 118826.
[28] H. Qi, R. Zuo, A. Xie, A. Tian, J. Fu, Y. Zhang, S. Zhang, *Adv. Funct. Mater.* **2019**, *29*, 1903877.
[29] P. Mohapatra, Z. Fan, J. Cui, X. Tan, *J. Eur. Ceram. Soc.* **2019**, *39*, 4735.
[30] H. Pan, M. Zhu, E. Banyas, L. Alaerts, M. Acharya, H. Zhang, J. Kim, X. Chen, X. Huang, M. Xu, I. Harris, Z. Tian, F. Ricci, B. Hanrahan, J. E. Spanier, G. Hautier, J. M. LeBeau, J. B. Neaton, L. W. Martin, *Nat. Mater.* **2024**, *23*, 944.
[31] G. Shirane, *Physcial Review* **1952**, *86*, 219.
[32] X. Hao, J. Zhai, L. B. Kong, Z. Xu, *Prog. Mater. Sci.* **2014**, *63*, 1.
[33] H. Shimizu, H. Guo, S. E. Reyes-Lillo, Y. Mizuno, K. M. Rabe, C. A. Randall, *Dalton Trans.* **2015**, *44*, 10763.
[34] Y. Z. Li, Z. J. Wang, Y. Bai, Z. D. Zhang, *J. Eur. Ceram. Soc.* **2019**, *40*, 1285.
[35] R. Gao, S. E. Reyes-Lillo, R. Xu, A. Dasgupta, Y. Dong, L. R. Dedon, J. Kim, S. Saremi, Z. Chen, C. R. Serrao, H. Zhou, J. B. Neaton, L. W. Martin, *Chem. Mat.* **2017**, *29*, 6544.
[36] B. P. Pokharel, D. Pandey, *J. Appl. Phys.* **2000**, *88*, 5364.
[37] X. Hao, J. Zhai, X. Yao, *J. Appl. Phys.* **2008**, *104*, 124101.
[38] H. Takenaka, I. Grinberg, S. Liu, A. M. Rappe, *Nature* **2017**, *546*, 391.
[39] J. Kim, H. Takenaka, Y. Qi, A. R. Damodaran, A. Fernandez, R. Gao, M. R. McCarter, S. Saremi, L. Chung, A. M. Rappe, L. W. Martin, *Adv. Mater.* **2019**, *31*, 1901060.
[40] Z. Tian, M. Xu, J. Kim, H. Pan, D. Lou, X. Huang, J. M. LeBeau, L. W. Martin, *Phys. Rev. Lett.* **2023**, *130*, 266801.

[41] A. Kumar, J. N. Baker, P. C. Bowes, M. J. Cabral, S. Zhang, E. C. Dickey, D. L. Irving, J. M. LeBeau, *Nat. Mater.* **2021**, *20*, 62.
[42] R. Li, D. Xu, M. Avdeev, L. Zhang, X. Chen, G. Gou, D. Wang, W. Liu, D. Zhou, *Adv. Funct. Mater.* **2023**, *33*, 2210709.
[43] F. Han, Y. Hu, B. Peng, L. Liu, R. Yang, K. Ren, *J. Eur. Ceram. Soc.* **2021**, *41*, 6482.
[44] X. Zhu, E. Defaÿ, G. Le Rhun, M. Aïd, Y. Xu, Q. Zhang, Y. Xiao, H. Gao, D. Liang, J. Zhu, J. Zhu, D. Xiao, *J. Appl. Phys.* **2012**, *112*, 54105.
[45] X. H. Zhu, B. Guigues, E. Defaÿ, C. Dubarry, M. Aïd, *J. Appl. Phys.* **2009**, *105*, 44108.
[46] M. W. Cole, E. Ngo, S. Hirsch, J. D. Demaree, S. Zhong, S. P. Alpay, *J. Appl. Phys.* **2007**, *102*, 34104.
[47] M. Falmbigl, I. S. Golovina, C. J. Hawley, A. V. Plokhikh, O. Shafir, I. Grinberg, J. E. Spanier, *Acta Mater.* **2021**, *208*, 116712.
[48] Y. J. Wang, H. C. Lai, Y. A. Chen, R. Huang, T. Hsin, H. J. Liu, R. Zhu, P. Gao, C. Li, P. Yu, Y. C. Chen, J. Li, Y. C. Chen, J. W. Yeh, Y. H. Chu, *Adv. Mater.* **2023**, 2304128.
[49] A. Ahmed, I. A. Goldthorpe, A. K. Khandani, *Appl. Phys. Rev.* **2015**, *2*, 011302.
[50] C. J. G. Meyers, C. R. Freeze, S. Stemmer, R. A. York, *Appl. Phys. Lett.* **2016**, *109*, 112902.
[51] A. Samanta, S. Yadav, Z. Gu, C. J. G. Meyers, L. Wu, D. Chen, S. Pandya, R. A. York, L. W. Martin, J. E. Spanier, I. Grinberg, *Adv. Mater.* **2022**, *34*, 2106021.
[52] M. Schaffer, B. Schaffer, Q. Ramasse, *Ultramicroscopy* **2012**, *114*, 62.
[53] M. W. Tate, P. Purohit, D. Chamberlain, K. X. Nguyen, R. Hovden, C. S. Chang, P. Deb, E. Turgut, J. T. Heron, D. G. Schlom, D. C. Ralph, G. D. Fuchs, K. S. Shanks, H. T. Philipp, D. A. Muller, S. M. Gruner, *Microsc. Microanal.* **2016**, *22*, 237.